Journal of Catalysis **194,** 91–104 (2000)
doi:10.1006/jcat.2000.2911, available online at http://www.idealibrary.com on IDEAL®

Characterization of Rh Particles and Li-Promoted Rh Particles in Y Zeolite during CO_2 Hydrogenation—A New Mechanism for Catalysis Controlled by the Dynamic Structure of Rh Particles and the Li Additive Effect

Kyoko K. Bando,*[,1] Nobuyuki Ichikuni,† Kensaku Soga,‡ Kimio Kunimori,‡ Hironori Arakawa,* and Kiyotaka Asakura§

*National Institute of Materials and Chemical Research, Higashi, Tsukuba, Ibaraki 305-8565, Japan; †Department of Applied Chemistry, Faculty of Engineering, Chiba University, Yayoi-cho, Inage, Chiba, Chiba 263-8522, Japan; ‡Institute of Materials Science, University of Tsukuba, Ten-noudai, Tsukuba, Ibaraki 305-8573, Japan; and §Catalysis Research Center, Hokkaido University, Kita-ku 11-10, Sapporo 060-0811, Japan

Received January 24, 2000; revised April 20, 2000; accepted April 20, 2000

The structure transformations of Rh particles in Rh ion-exchanged zeolite catalysts (RhY) and in Li-doped RhY catalysts (Li/RhY) were studied by means of EXAFS (extended X-ray absorption fine structure) in order to reveal the origin of the different CO_2 hydrogenation catalyses of the two catalysts. CH_4 was mainly produced from $CO_2 + H_2$ on RhY, while CO was found on Li-doped RhY under similar reaction conditions. The geometric and electronic structure of Rh species in Y zeolite had little difference between the two catalysts before the reaction. However, EXAFS revealed that the structures of Rh species under the reaction conditions were quite different. During the reaction, we found disassembly of Rh particles in RhY, while Rh particles were stably present in Li/RhY. We discuss the different reaction mechanisms and catalytic properties of RhY and Li-doped RhY catalysts on the basis of their different dynamic structures which might be controlled by Li additive.

Key Words: **CO_2 hydrogenation; Li additive; Rh ion-exchanged zeolite; EXAFS.**

1. INTRODUCTION

In order to recycle disposed CO_2 as a resource (1) and to limit global climate change due to the greenhouse effect caused by CO_2 emission (2), it is desirable to develop efficient technology for both mitigation and utilization of CO_2. CO_2 hydrogenation to form valuable chemicals like oxygenates and/or higher hydrocarbons is one example. It is well known that supported Rh catalysts show high efficiency for oxygenate production from $CO + H_2$ (3). Intensive work has been done on CO_2 hydrogenation over impregnated Rh catalysts (4). It has been clarified that this reaction is intermediated by adsorbed CO species (4, 5). Under ambient pressure, methane was exclusively produced (6), while formation of CO and alcohol was observed under elevated pressure (7).

We have been engaged in investigations on the CO_2 hydrogenation reactivity of Rh ion-exchanged Y-type zeolite catalysts (RhY) (8). We reported that RhY showed extraordinarily high activity in CO_2 hydrogenation, producing methane with almost 100% selectivity (reaction conditions: $CO_2/H_2 = 1/3$, total pressure = 3 MPa, flow rate = 100 ml/min, and reaction temperature = 523 K). It has been reported that alkali additives greatly modify product selectivity in CO/CO_2 hydrogenation (9, 10) and in certain cases, promotion of oxygenate formation is observed. Therefore, we prepared Li-doped RhY (Li/RhY) and investigated its reactivity toward CO_2 hydrogenation. Interestingly, the addition of Li dramatically changed the reactivity of RhY catalysts (11). CH_4 production was completely suppressed and CO was mainly formed on Li/RhY. Usually the origin of Li modification of the catalysis is attributed to an electronic effect or the formation of a new Rh–Li ensemble (12). We have carried out XPS and XRD measurements to find the difference between RhY and Li/RhY (11). However, no notable difference was observed either in the binding energy of Rh or in the size of Rh particles. In this work, we carried out CO/H_2 adsorption, TEM, and EXAFS experiments. There was also little difference in initial structure between two catalysts. However, EXAFS observation of the working catalysts showed that the dynamic structures of Rh species were quite different between RhY and Li/RhY under the reaction conditions. We will propose a new dynamic control mechanism for the Rh catalysis by addition of Li.

2. EXPERIMENTAL

A zeolite-supported Rh catalyst was prepared by an ion-exchange method according to the literature as explained

[1] To whom correspondence should be addressed. Fax: +81-298-61-4534. E-mail: bando@nimc.go.jp.

0021-9517/00 $35.00

elsewhere (8). The support used in this work was the NaY-type zeolite (SK-40, Nishio, Si/Al = 2.3 (atomic ratio)). $RhCl_3 \cdot 3H_2O$ (Wako, 99.5%) was used as a Rh precursor for ion exchange. After ion-exchange treatment the catalyst was calcined at 673 K for 6 h under flow of dry air (100 ml/min). The catalyst thus obtained is denoted as RhY. An Li-promoted catalyst was prepared by an incipient impregnation method. The calcined RhY catalyst was dried at 473 K for 1 h under vacuum; then an adequate amount of aqueous solution of $LiNO_3$ was poured onto the RhY catalyst. The catalyst was then calcined again at 673 K for 6 h under dry air. This catalyst is abbreviated as Li/RhY. The concentration of Rh supported on the zeolite was estimated from the amount of Rh remaining in the filtrated solution, which was determined by atomic absorption spectrometry (SEIKO SAS760). The determined loading of Rh was about 5 wt%. The extent of ion exchange was 49%.

The CO_2 hydrogenation reaction was carried out on a fixed-bed flow reactor. One gram of a catalyst was set in the reactor and was reduced at 723 K for 0.5 h under the flow of H_2 (100 ml/min). After cooling to ambient temperature, the H_2 gas was exchanged with premixed reactant gas ($H_2/CO_2 = 3$ and 1% of Ar was included as an internal standard). The reaction was conducted under the following conditions: total pressure = 3 MPa, temperature = 523 K. Effluent gas was analyzed by online gas chromatographs equipped with four kinds of column: 2% squalane/activated carbon, VZ-10, 10% PEG1500/Silimate TPA, and 10% PEG6000/silimate TPA.

The catalysts reduced at 723 K for 1 h are called "fresh." The "used" catalysts were prepared by conducting the CO_2 hydrogenation reaction at 523 K for 1 h, followed by reduction at 723 K with H_2.

The ratio of surface to total Rh atoms (dispersion) was determined by volumetric H_2 adsorption assuming a stoichiometry of H/Rh (surface) = 1. A sample was prereduced at 723 K for 0.5 h under a flow of H_2 (100 ml/min). Subsequently, it was evacuated at 673 K for 1–2 h. After the catalyst was cooled to room temperature, the adsorption isotherm of H_2 was measured up to 7 kPa at room temperature and the amount of adsorbed hydrogen was obtained by extrapolating the adsorption isotherm to 0 kPa. CO adsorption was also conducted to estimate the abilities of Rh sites to adsorb CO. The pretreatment procedure was the same as that for the H_2 adsorption.

The particle size and shape of the catalyst were also monitored by TEM at an accelerating voltage of 400 kV (JEOL JEM-4000FXII). The samples were reduced under a H_2 flow for 0.5 h at 723 K prior to the observation. They were then suspended in 2-propanol using an ultrasonic wave. The finest part of the suspension was dropped onto a copper microgrid covered with Collodion film (200 mesh, Nisshin EM Co., Ltd.).

Rh *K*-edge EXAFS spectra were measured in the transmission mode at BL-10B in the Photon Factory of the Institute of Materials Structure Science, High Energy Accelerator Research Organization (PF-IMSS-KEK). The storage ring was operated at 2.5 GeV and 300 mA. The synchrotron radiation was monochromatized by an Si(311) channel-cut monochromator. The energy resolution was 7 eV. The incident and transmitted X-rays were monitored by I_0 and I ionization chambers filled with Ar and Kr, respectively. Calibration of the monochromator was carried out by adjusting the energy of the Rh *K*-edge, observed for Rh foil as 23219.8 eV. Samples were treated in a closed circulating system and transferred to a bronze cell with Kapton windows without exposure to air. The measurements were performed at low temperature (70 K) using a closed He circulating cryostat. Samples in the working state were prepared and measured in a different way. The reaction was quenched by reducing the pressure of the reactants. After the reactor was cooled to room temperature, it was sealed by two stop valves and was put in an N_2-filled glove box. In the glove box, the sample was packed in a polyethylene film bag which was then sealed by a hot press to keep the sample in a N_2 atmosphere. The EXAFS spectra were measured at ambient temperature.

The analysis of observed EXAFS oscillations was conducted as follows: the background was removed from the observed spectrum by a cubic smoothing method and the extracted oscillation was normalized by the edge height. The k^3-weighted EXAFS was Fourier transformed over $k = 30$–160 nm^{-1}. Inversely Fourier-transformed data for each Fourier peak were analyzed by a curve-fitting method. Curve-fitting analyses of EXAFS oscillations were conducted by an EXAFS analysis program, REX (Rigaku Co.), using the formula (13)

$$\chi(k) = \sum_j N_j F_j(k'_j) \exp(-2k'^2_j \sigma_j^2) \sin(2k'_j r_j + \phi_j(k'_j))/k'_j r_j^2$$
$$k'_j = \sqrt{k^2 - 2m\Delta E_j/\hbar}, \qquad [1]$$

where k is the photoelectron wave number and $F_j(k)$ and $\phi_j(k)$ are the backscattering amplitude and the phase shift function, respectively. The backscattering amplitude and phase shift functions for Rh–Rh and Rh–O bonds were extracted from oscillations observed for model compounds (Rh foil and Rh_2O_3, respectively) measured at corresponding temperatures. N_j, σ_j, ΔE_j, and r_j represent the coordination number, the Debye–Waller factor, the difference in the origin of photoelectron kinetic energy between a reference and an unknown compound, and the interatomic distance for the jth shell, respectively. N_j, σ_j, ΔE_j, and r_j are used as fitting parameters.

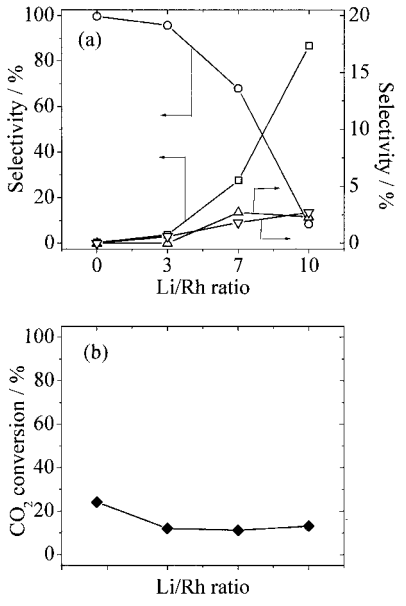

FIG. 1. The result of CO_2 hydrogenation over Li-doped RhY catalysts (Li/Rh = 0–10, in atomic ratio). Reaction conditions: catalyst = 1 g, $H_2/CO_2 = 3$, total pressure = 3 MPa, flow rate = 100 ml/min. (a) Selectivity for CH_4 (○), CO (□), CH_3OH (△), and C_2H_5OH (▽); (b) CO_2 conversion.

3. RESULTS

3.1. CO_2 Hydrogenation Reaction

Figure 1 shows the results of the CO_2 hydrogenation reaction carried out over Rh ion-exchanged zeolite catalysts (RhY) with various amounts of Li additive. As the amount of Li additive increases, the main product alters from methane to CO (Fig. 1a), retaining the same level of total conversion (Fig. 1b). When the amount of added Li was Li/Rh = 10 in atomic ratio, the selectivity for CO reached 87% and promotion of alcohol production was also observed (methanol = 2.3% and ethanol = 2.7%).

3.2. H_2 and CO Adsorption

We carried out H_2 and CO adsorption experiments for RhY and Li/RhY. The samples used in this experiment were all fresh ones. The amount of doped Li was set at Li/Rh (an atomic ratio between Li atoms and Rh atoms) = 0, 5, and 10. The results are shown in Table 1. The value of H/Rh (the atomic ratio between the adsorbed hydrogen atoms and the total Rh atoms) decreases a little as the Li/Rh value increases. If we assume a spherical model, the calculated particle sizes are 1.2 nm, 1.2 nm, and 1.5 nm for the samples of Li/Rh = 0, 5, and 10, respectively. This result is consistent with our previous XRD experiments; that is, we could not obtain a discernible diffraction peak attributed to Rh particles in the XRD patterns (11). The results of CO adsorption for the catalysts (Li/Rh = 0, 5, 10) are also shown in Table 1. The value of CO/Rh greatly decreases with the increase of Li/Rh. The ratio between H/Rh and CO/Rh (CO/H for short) is not identical among the samples with different Li loadings. The CO/H value decreases as the Li/Rh value increases. The CO/H ratio exceeds 1, indicating the multiple adsorption of CO on RhY. These facts imply that the multiple adsorption of CO is suppressed by Li addition onto Rh particles as predicted in our previous work (11), where IR spectra indicated that twin-type CO adsorbates decreased with increased Li content and terminal and bridged CO species became predominant on Li/RhY.

TABLE 1

Results of H_2 and CO Adsorption

Amount of doped Li, Li/Rh	Amount of adsorbed species		Ratio of adsorbed species, CO/H
	CO/Rh	H/Rh	
0	1.54	0.95	1.62
5	1.01	0.92	1.10
10	0.58	0.75	0.77

Note. All the values are expressed as atomic ratio.

3.3. TEM Observations

Figures 2a and 2b show the TEM observation of fresh and used RhY catalysts (8). We found that, before the reaction, the Rh particles were as large as about 1.3 nm in diameter (Fig. 2a). They became larger (about 3.3 nm in diameter) after a CO_2 hydrogenation reaction as shown in Fig. 2b.

Figure 2c depicts an image observed for the fresh Li/RhY catalyst. Large particles were observed on the external surface with an average diameter of about 3.0 nm. Figure 2d shows a TEM picture of the used Li/RhY catalyst. The average particle size of Li/RhY after the reaction was unvaried at 3.0 nm in diameter. These facts suggest that the particles observed by TEM may be relatively large and appear to be the same size before and after the reaction. However, these results conflict with those of H_2 and CO adsorption and XRD, which show the presence of particles much smaller than 3.0 nm.

3.4. EXAFS

3.4.1. EXAFS analysis on RhY and Li/RhY. We carried out EXAFS measurements of the Rh particles in order to obtain detailed information about the interaction between Li and Rh. The Li content was set at Li/Rh = 10 (atomic ratio). Figure 3 depicts k^3-weighted EXAFS oscillations ($k^3\chi(k)$) and Fourier transforms of $k^3\chi(k)$ for fresh RhY and Li/RhY samples. We found a main peak around 0.24 nm in all Fourier transforms, and it was assigned to a Rh–Rh bond. No peak attributed to a Rh–Li bond could be observed. The inversely Fourier-transformed data were analyzed by the curve-fitting method. The range of inverse Fourier transformation was 0.18–0.30 nm for the first shell. The fitting range was 30–160 nm^{-1}. The phase shift and amplitude functions were derived from the Rh foil.

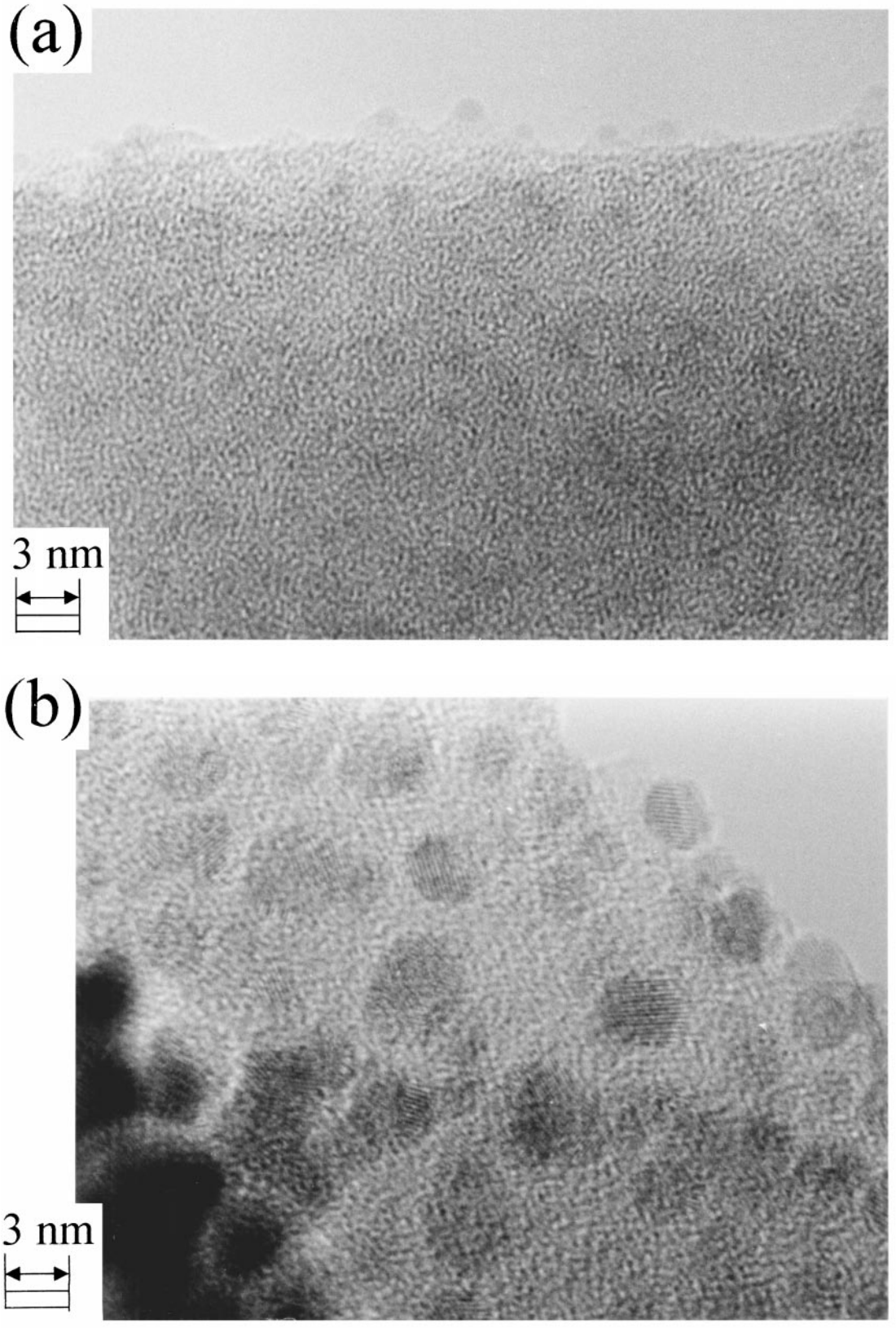

FIG. 2. TEM images of the RhY ((a) fresh and (b) used) and the Li/RhY catalyst (Rh = 5 wt%, Li/Rh = 10) ((c) fresh and (d) used). All of them were pretreated under H_2 at 723 K for 0.5 h before measurement.

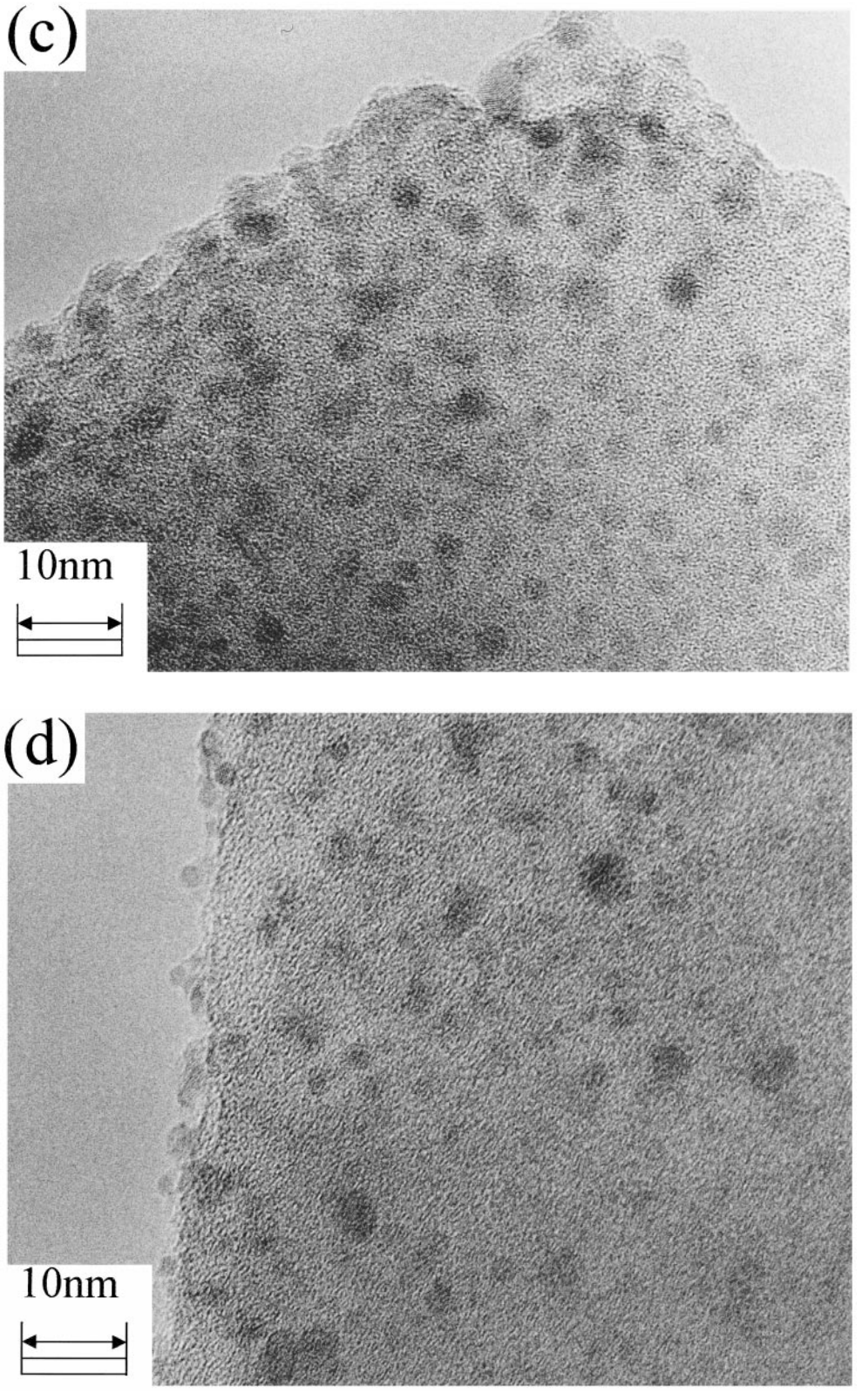

FIG. 2—*Continued*

TABLE 2

Curve-Fitting Results for EXAFS Oscillations

Sample name	Sample	Pretreatment	Bonding	CN	Distance/0.1 nm	ΔE/eV	σ/0.1 nm	R factor/%	Observed temp/K
Sample 1	Fresh RhY	H_2 reduction[a]	Rh–Rh	7.6 ± 1.2	2.66	11	0.082	0.75	70
Sample 2	Fresh RhY	CO adsorption[b]	Rh–Rh	4.2 ± 0.8	2.69	2.7	0.076	1.06	70
Sample 3	Used RhY	H_2 reduction[a]	Rh–Rh	10.3 ± 3.0	2.67	1.72	0.077	0.78	70
Sample 4	Used RhY	CO adsorption[b]	Rh–Rh	8.3 ± 2.7	2.68	0.57	0.073	0.66	70
Sample 5	Used RhY	$CO_2 + H_2$[c]	Rh–Rh	4.6 ± 1.0	2.69	2.7	0.083	0.96	293
			Rh–O	2.6 ± 1.2	2.01	−2.8	0.072		
Sample 6	Fresh Li/RhY	H_2 reduction[a]	Rh–Rh	7.0 ± 1.4	2.67	4.8	0.085	0.89	70
Sample 7	Fresh Li/RhY	CO adsorption[b]	Rh–Rh	6.0 ± 1.0	2.68	2.2	0.078	0.83	70
Sample 8	Used Li/RhY	H_2 reduction[a]	Rh–Rh	8.7 ± 2.0	2.67	1.9	0.083	0.79	70
Sample 9	Used Li/RhY	CO adsorption[b]	Rh–Rh	7.1 ± 1.0	2.68	1.1	0.077	0.41	70
Sample 10	Used Li/RhY	$CO_2 + H_2$[c]	Rh–Rh	7.0 ± 1.0	2.70	−0.57	0.081	1.3	293

Note. Rh = 5 wt%, Li/Rh = 10 (atomic ratio), fitting range = 30–160 nm^{-1}, Fourier filter range = 0.19–0.30 nm.

[a] After H_2 reduction for 1 h at 723 K, then H_2 gas was evacuated.

[b] After H_2 reduction for 1 h at 723 K, about 13 kPa of CO was introduced on the catalysts for 10 min, and then the catalyst was evacuated.

[c] $CO_2 + H_2$ reaction (523 K, $H_2/CO_2 = 3$, total pressure = 3 MPa, flow rate = 200 ml/min).

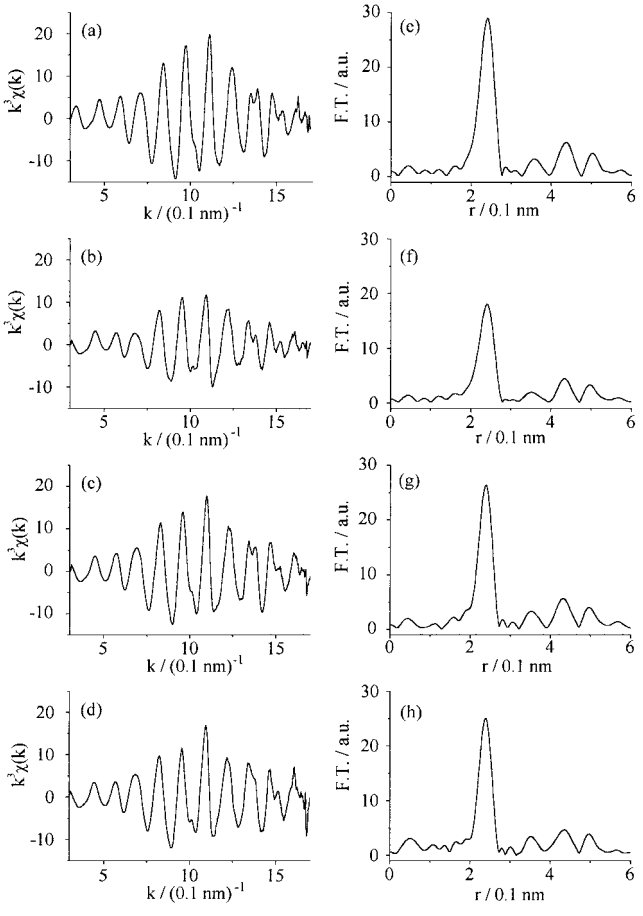

FIG. 3. EXAFS oscillations ($k^3\chi(k)$) (a–d) and their Fourier transforms (e–h) observed for the fresh RhY and Li/RhY catalysts. (a and e) RhY after H_2 reduction (sample 1); (b and f) RhY after CO adsorption (sample 2); (c and g) Li/RhY after H_2 reduction (sample 6); (d and h) Li/RhY after CO adsorption (Sample 7). H_2 reduction conditions: 723 K, 0.5 h. CO adsorption: $P_{CO} = 13$ kPa, ambient temperature. The Rh loading was 5 wt%. Li/Rh was 10 for the Li/RhY catalyst.

Table 2 shows the curve-fitting results for the first shell. As for the fresh RhY (Sample 1 in Table 2), a coordination number (CN) for the first shell Rh was 7.6. The R factor defined in the following equation was less than 2% for the first shell, as shown in Table 2:

$$R = \sqrt{\sum(\chi_{obs} - \chi_{cal})^2 \Big/ \sum \chi_{obs}^2} \qquad [2]$$

There are three more peaks appearing at 0.38, 0.43, and 0.51 nm in Fourier-transformed spectra (Fig. 3). These peaks mainly consist of scattering from the second, third, and fourth neighboring Rh atoms in Rh metal particles with fcc structure, respectively. We carried out curve-fitting analysis of each shell using inversely Fourier-transformed data observed for the fresh RhY (sample 1). The ranges of inverse Fourier transformation were 0.32–0.40, 0.39–0.47, and 0.47–0.53 nm for the second, third, and fourth shells, respectively. Model parameters for the curve-fitting analysis were extracted from the spectrum observed for Rh foil. The results are shown in Table 3 (sample 1). R factors were within 4%. Table 3 also involves coordination numbers calculated from model structures of Rh particles as shown in Fig. 4. Figure 4 depicts typical three models of spherical shape with different sizes (a, b, c) The observed data correspond well to those calculated for a spherical model (Fig. 4a, model 3) of particle size 1.3 nm.

Figures 3c and 3g show the k^3-weighted EXAFS oscillation and its Fourier transform for the fresh Li/RhY. In this spectrum higher shells (second, third, and fourth) can be seen as in the case of the fresh RhY. A curve-fitting result for the first shell is given in Table 2 as sample 6. The R factor for the first shell is as good as that in RhY. Thus the contribution of the Li–Rh bond, if any, is too small to be detected by EXAFS. The coordination numbers for the first,

TABLE 3

Curve-Fitting Results of First, Second, Third, and Fourth Shells Observed for the Fresh RhY (Sample 1) Together with Calculated Coodination Numbers for Models

Sample/model name	Sample	Coordination number			
		1st shell	2nd shell	3rd shell	4th shell
Sample 1	Fresh reduced RhY	7.6	2.2	6.8	4.3
Model 1	Rh metal	12	6	24	12
Model 2	3.0-nm spherical model	10.4	4.9	18.4	8.9
Model 3	1.3-nm spherical model[a]	7.9	3.3	9.6	4.1

[a] Including 55 Rh atoms as shown in Fig. 4a.

second, third, and fourth shells of the fresh Li/RhY were determined to be 7.0, 2.0, 4.8, and 3.0, respectively. Table 4 shows the results of curve-fiitting analysis for higher shells together with those calculated for several structure models. The 3.0 nm particle model shown in Table 4 expected from TEM results could never reproduce the observed coordination numbers given by EXAFS. This inconsistency will be discussed later.

3.4.2. Structure change induced by CO adsorption on Rh particles. When CO was adsorbed on the fresh Rh/Y, the peak due to the Rh–Rh bond decreased significantly (Figs. 3e → 3f), and the coordination number fell to 4.2 (Table 2, sample 2). The Rh–Rh distance was 0.269 nm, similar to that in the Rh metal particles. This suggests partial decomposition of Rh particles into an atomically dispersed form in the surface reaction

$$[\mathrm{Rh}]_n + 2\mathrm{CO} + x\mathrm{HO}^- \rightarrow [\mathrm{Rh}]_{n-1} + \mathrm{Rh(CO)_2(O)}_x + (x/2)\mathrm{H_2}. \quad [3]$$

Similar disruption of Rh–Rh bonding upon CO adsorption onto highly dispersed Rh particles supported on Al_2O_3 has been reported and thoroughly studied in the literature (14, 15).

On the other hand, for the fresh Li/RhY, the peak at 0.24 nm decreased little upon CO adsorption (Figs. 3g → 3h). The curve-fitting analysis gave a coordination number of 6.0 for CO-adsorbed Rh particles (sample 7) which was slightly less than that for the fresh Li/RhY before CO adsorption (sample 6), suggesting that a minor decomposition reaction [3] occurred in Li/RhY upon CO adsorption and the Rh particle structure is rather robust.

3.4.3. EXAFS of the used catalysts. After the CO_2 hydrogenation reaction and the subsequent H_2 reduction, the peak height at 0.24 nm in the Fourier transform became larger in the used RhY (sample 3, Fig. 5e) than that in the fresh RhY (sample 1, Fig. 3e). The coordination number for the first shell became 10.3. Figure 6 shows changes in the coordination numbers for the first to the fourth shells resulting from the several treatments. The coordination numbers of all the neighboring shells in Rh particles in RhY increased after the reaction. The increase in coordination numbers in the higher shells was larger than that in the first shell, indicating the formation of larger particles. Assuming a spherical shape, the particle size estimated from coordination numbers was determined to be 3 nm, which agreed well with the value estimated from TEM (3.3 nm) (8). It is suggested that the CO_2 hydrogenation reaction and subsequent reduction forced Rh atoms to leave the cages and to form large Rh particles on the external surface of the zeolite.

On the other hand, in Li/RhY, we found a small increase in the coordination number of the first shell Rh–Rh bond (sample 8, CN = 8.7) after the reaction, compared to that

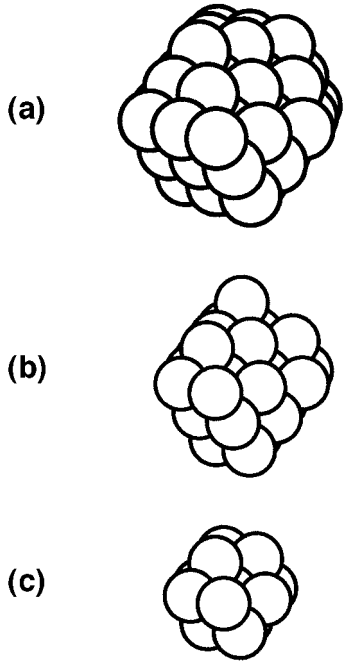

FIG. 4. Models for Rh particles. (a) model 3, a spherical model 1.3 nm in diameter, 55 Rh atoms; (b) model 4, a spherical model 1.0 nm in diameter, 28 Rh atoms; and (c) model 5, a spherical model 0.8 nm in diameter, 13 Rh atoms.

TABLE 4

Curve-Fitting Results of First, Second, Third, and Fourth Shells Observed for the Fresh Li/RhY (Sample 6) Together with Calculated Coodination Numbers for Models

Sample/model name	Sample	Coordination number			
		1st shell	2nd shell	3rd shell	4th shell
Sample 6	Fresh reduced Li/RhY	7.0	2.0	4.8	3.0
Model 2	3.0 nm spherical model	10.4	4.9	18.4	8.9
Model 3	1.3 nm spherical model[a]	7.9	3.3	9.6	4.1
Model 4	1.0 nm spherical model[b]	6.8	2.7	6.8	2.7
Model 5	0.8 nm spherical model[c]	5.5	1.8	3.7	0.92
Model 6	10% Model 2 + 90% Model 5	6.1	2.2	5.5	1.9

[a] Including 55 Rh atoms as shown in Fig. 4a.
[b] Including 28 Rh atoms as shown in Fig. 4b.
[c] Including 13 Rh atoms as shown in Fig. 4c.

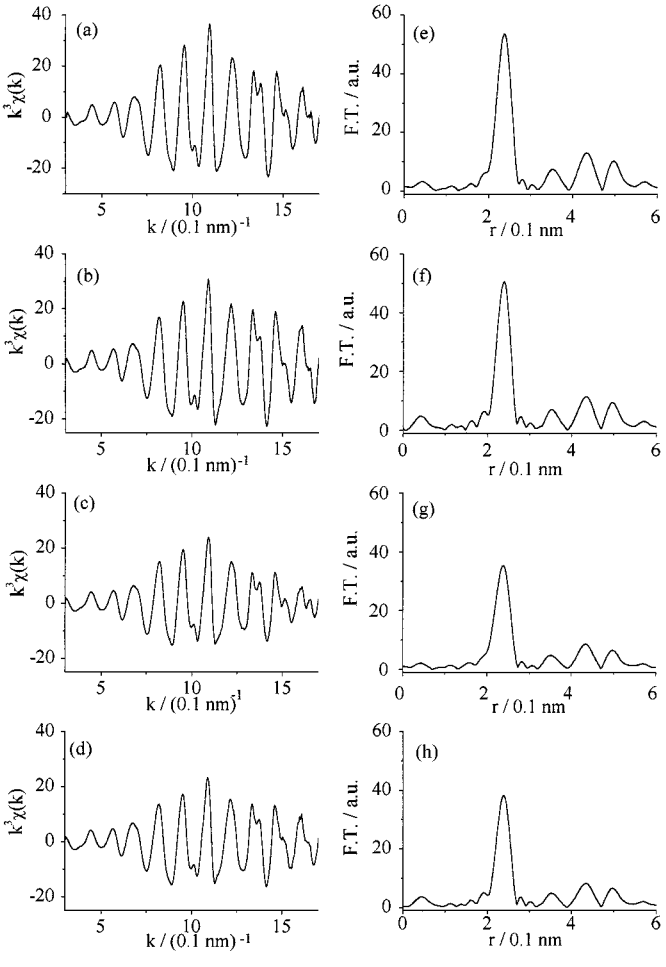

FIG. 5. EXAFS oscillations ($k^3\chi(k)$) (a–d) and their Fourier transforms (e–h) observed for the used RhY and Li/RhY catalysts. (a and e) RhY after H_2 reduction (sample 3); (b and f) RhY after CO adsorption (sample 4); (c and g) Li/RhY after H_2 reduction (sample 8); (d and h) Li/RhY after CO adsorption (Sample 9). H_2 reduction conditions: 723 K, 0.5 h. CO adsorption: $P_{CO} = 13$ kPa, ambient temperature. The Rh loading was 5 wt%. Li/Rh was 10 for the Li/RhY catalyst.

for the fresh material (sample 6, CN = 7.0), indicating that the Li additive suppressed the aggregation of Rh particles during the reaction.

3.4.4. CO adsorption on used RhY and Li/RhY. Figures 5f and 5h show the Fourier transforms of EXAFS oscillations ($k^3\chi(k)$) for the used RhY and Li/RhY after CO adsorption (samples 4 and 9). The main peak in RhY (sample 4) decreased compared with the one for the reduced sample (sample 3). The coordination number in the first shell was 8.3 and it was smaller than the number before CO adsorption (sample 3). The reduction in the coordination number was not large compared to the corresponding change in the coordination number of the fresh samples (samples 1 and 2) accompanied by CO adsorption. Although partial destruction of Rh particles occurred, the extent of the degradation of the Rh particles was smaller than that in the fresh samples (Section 3.4.2). This

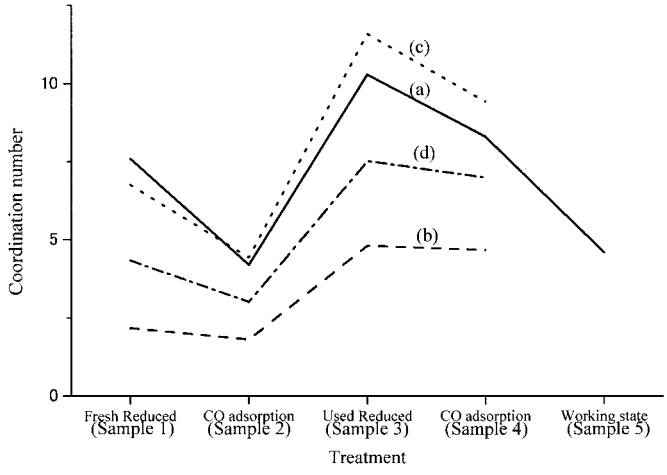

FIG. 6. Change in coordination numbers for RhY with treatments. (a) The first shell, (b) the second shell, (c) the third shell, and (d) the fourth shell.

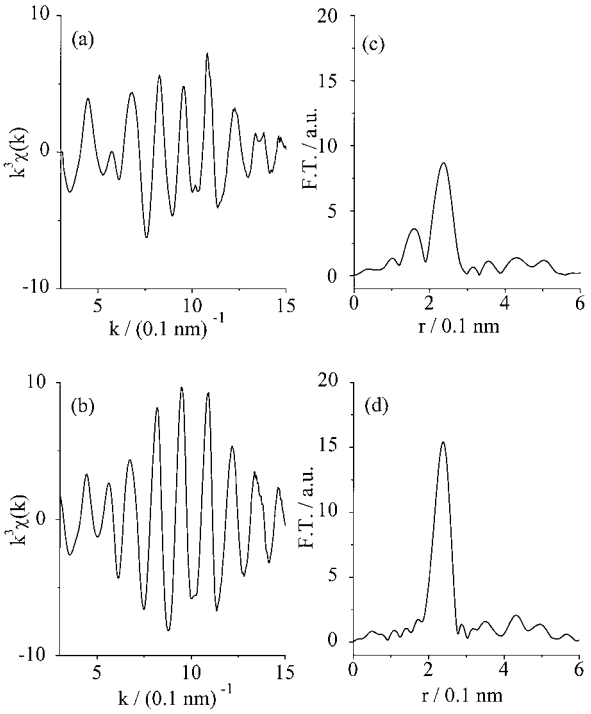

FIG. 7. EXAFS oscillations ($k^3\chi(k)$) (a and b) and their Fourier transforms (c and d) observed for the RhY and Li/RhY catalysts in the working state. (a and c) for RhY (sample 5); (b and d) for Li/RhY (sample 10).

suppression of CO-induced Rh disruption is not due to deposition of carbon on the Rh surface (4), which would prevent CO from adsorbing onto the Rh atom, because the catalyst was subjected to H_2 reduction at 723 K before CO adsorption, at which all carbon was converted to CH_4. It is rather due to the larger size of the Rh particles (sample 3) compared to those on the fresh catalyst (sample 1). It is reported that the CO-induced degradation of Rh particles forming isolated Rh gem-carbonyls becomes slower as the initial size of the Rh particles becomes larger (16, 17). Table 2 shows the coordination number of the first shell of the Rh–Rh bond in the used Li/RhY, which showed a small decrease upon CO adsorption, similar to the case of the fresh Li/RhY (samples 8 and 9).

3.4.5. EXAFS analysis of the catalysts in the working state. We conducted an EXAFS observation to see the structure of the sample under the reaction conditions upon the quenching of the reactions. Figure 7 shows the k^3-weighted EXAFS oscillations and their Fourier transforms for RhY and Li/RhY in the working state. Results of the curve-fitting analysis are given in Table 2 (samples 5 and 10). For the Li/RhY (sample 10), no new peak appeared in the Fourier transform, as shown in Fig. 7d. The coordination numbers of the first shell Rh–Rh, being 7.0, did not change compared with those in the fresh Li/RhY (sample 6). The Rh atoms in Li/RhY are so firmly bound to each other that they kept their structure unchanged during the reaction. On the other hand, a new peak appeared at 0.19 nm in the Fourier transform of RhY (sample 5) with a decrease in the Rh–Rh peak during the reaction. We conducted two shell curve-fitting analyses on the inversely Fourier transformed data over 0.1–0.3 nm. The fitting range was 30–150 nm^{-1}. The number of degrees of freedom in the fitting was calculated as 18 ($\approx 2\Delta r\,\Delta k/\pi + 2 = 2 \times 0.2 \times 120/\pi + 2$) and was larger than the number of fitting parameters (8 in this case). The new peak was assigned to Rh–O bonding. The coordination numbers of Rh–O and Rh–Rh were 2.6 and 4.6, respectively (Table 2). This fact indicates the disruption of the Rh–Rh bond and the presence of highly dispersed oxidized Rh atoms in the RhY. Thus addition of Li has stabilized the Rh particle structure during the CO_2 hydrogenation reaction even at high temperature and under high pressure.

3.5. XANES Spectra

X-ray absorption near-edge structure (XANES) is sensitive to the local electronic and geometric changes of an X-ray absorbing atom. Because X-rays at the Rh *K*-edge region can penetrate deeply into the material, XANES can detect the change in the electronic state of Rh particles inside the zeolite, in contrast to XPS, in which the information about the Rh species on the external surface of the zeolite may be dominant. Figure 8 shows the XANES spectra

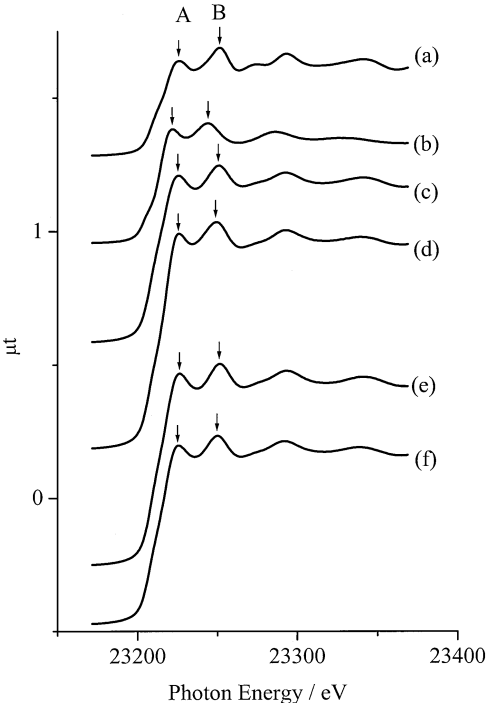

FIG. 8. XANES spectra observed for (a) Rh foil, (b) $Rh_6(CO)_{16}$, (c) fresh RhY (sample 1), (d) fresh RhY after CO adsorption (sample 2), (e) fresh Li/RhY (sample 6), and (f) fresh Li/RhY after CO adsorption (sample 7).

observed for the fresh RhY and Li/RhY catalysts together with those after CO adsorption. The XANES of Rh foil is composed of a smaller edge peak A and a larger peak B followed by EXAFS oscillations. If the Rh atom is negatively (positively) charged, the edge will shift to lower (higher) energy. Figures 8a and 8b show the XANES spectra observed for Rh foil and $Rh_6(CO)_{16}$, respectively. It can be seen that the interval between the peaks A and B (22.7 eV) becomes narrower for $Rh_6(CO)_{16}$ than that found in the Rh foil (25.2 eV). In the spectra observed for the fresh RhY (sample 1, Fig. 8c) and Li/RhY (sample 6, Fig. 8e), little difference was found in edge position and peak intensities, compared to those of the Rh foil. This fact indicates that the Li additive little affects the electronic state of Rh particles in Li/RhY and RhLi alloy particles are not formed in Li/RhY. When CO was adsorbed on the Rh particles in RhY, the position of the peak A was almost unchanged, while the peak B shifted by 2 eV to lower energy. That is, the interval between the peaks A and B decreased from 26 eV (Fig. 8c) to 24 eV (Fig. 8d), indicating the partial formation of Rh carbonyl species. On the other hand, in Li/RhY, the interval between the peaks A and B decreased only by 0.7 eV on CO adsorption (Figs. 8e $\rightarrow$ 8f). CO has less influence on the Rh particle structure in Li/RhY.

Figure 9 shows the Rh *K*-edge XANES spectra of RhY and Li/RhY (sample 5 and sample 10) in the working state. In the spectrum of Li/RhY in the working state (sample 10, Fig. 9b), we cannot find any notable change compared to the spectrum of the fresh catalyst shown in Fig. 8e. On the other hand, the XANES spectrum for RhY in the working state (sample 5) significantly changes upon the $CO_2 + H_2$ reaction as shown in Fig. 9a. The intensity of the first peak becomes stronger. Comparing to the XANES spectrum of Rh_2O_3 in Fig. 9c, we assign the change in the spectra to a generation of partially oxidized Rh species.

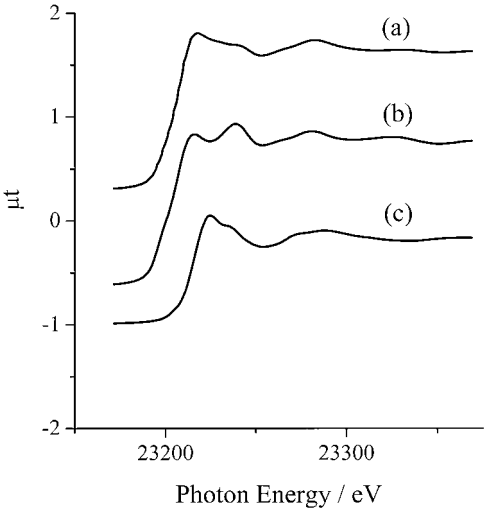

FIG. 9. XANES spectra observed for (a) RhY in the working state (sample 5), (b) Li/RhY in the working state (sample 10), and (c) Rh_2O_3.

4. DISCUSSION

As mentioned in Section 3.1, addition of Li alters the main product from methane to CO and the effect of Li cannot be explained as a simple blocking of active Rh sites. First, we discuss the surface structure of the catalysts.

4.1. Li Effect on the Structure of Rh Particles

4.1.1. Structure of reduced fresh Rh/Y and Li/RhY. XPS, EXAFS, and XANES results indicate that the Rh atom is present in a metallic state in the fresh RhY (sample 1). According to the TEM results, the Rh particle size is initially 1.3 nm, which is almost the same as a supercage diameter of NaY (8). XPS observation of the fresh RhY catalyst (sample 1) indicates that the Rh atoms are uniformly dispersed inside the cages (11). Thus we conclude that the Rh metal particle is present inside the supercage of Y zeolite. EXAFS analyses on Pt, Pd, and Cu in Y zeolite prepared by ion-exchange in the literature show that the coordination number of the particles in the Y zeolite supercage is around 6–7 (18, 19), which corresponds well to the coordination number obtained for Rh particles in this work (=7.6). The analyses on higher coordination shells support this structure. On the other hand, the structure of Rh particles in Li/RhY is complicated. TEM depicts the presence of 3.0 nm Rh particles, though the XRD cannot detect such a large particle and the particle size estimated from H_2 adsorption is 1.5 nm. A 3.0-nm particle size model cannot reproduce the observed coordination numbers determined by EXAFS as shown in Table 4. One of the possible explanations for this disagreement in particle size might be LiRh alloy formation, which causes the modification of adsorption properties and disorder in Rh particles. It is often observed in EXAFS analyses that incorporation of an impurity induces lattice mismatch which increases disorder in metal–metal bonding and gives a smaller apparent coordination number. Tomishige *et al.* observed the decrease in the coordination number with the increase of the Sn content in the Rh–Sn alloy particles on the SiO_2, though the particle size slightly increased with the Sn content (20, 21). At the same time, they found an increase in the Debye–Waller factor of the Rh–Rh bond. They concluded that the decrease in the coordination number was not due to the particle size effect but was due to the disorder effect which was created by the mismatch of the Rh–Rh and Rh–Sn bond lengths. The small disorder effect can be compensated for by the Debye–Waller factor. But a large disorder can no longer be expressed by the Debye–Waller factor completely due to the asymmetric distribution effect and this reduces the coordination number. According to this idea, the reduction in the coordination number of Li/RhY is supposed to be attributed to the formation of Rh–Li alloy particles on the external surface of the zeolite. But this model cannot be

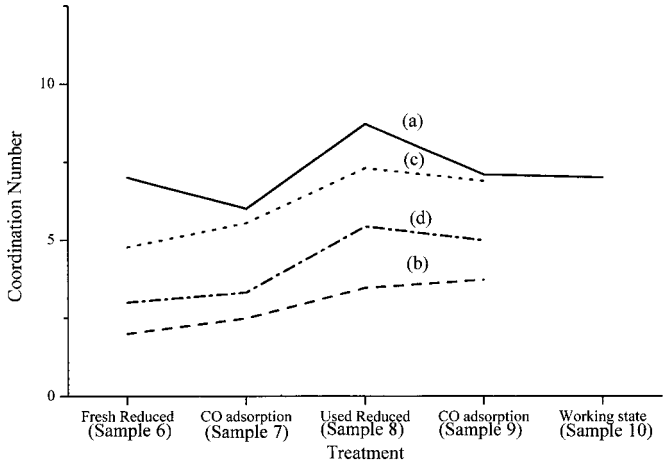

FIG. 10. Transformation of coordination numbers for Li/RhY. (a) The first shell, (b) the second shell, (c) the third shell, and (d) the fourth shell.

applied to our system for the following reasons:

(1) We could not find any remarkable increase in the Debye–Waller factors in the curve-fitting analysis, which are 0.0082 and 0.0085 nm for the Rh–Rh bonds of sample 1 and sample 6, respectively, as shown in Table 2.

(2) The disorder effect strongly affects the higher shell interactions; namely, the higher shells should remarkably diminish with the disorder. But the higher shells are clearly seen in Fourier transforms for sample 6 (Fig. 3g).

(3) Little change in XANES spectra (Figs. 8c and 8e) upon Li addition also does not indicate a direct Li–Rh interaction.

(4) We could not observe any contribution of a Rh–Li bond in the EXAFS spectra.

The second possible explanation is that the Rh species observed by TEM and EXAFS are different. TEM cannot detect a particle smaller than 1.0 nm, though all Rh species contribute EXAFS spectra. We postulate that there are two kinds of Rh particles in Li/RhY. One is a small Rh cluster, which is about 0.8 nm (about 13 Rh atoms) in diameter and is encapsulated in the cage. Such a particle is invisible to TEM. The other is a large particle, which is estimated to be as large as 3 nm in diameter and is observed with TEM. On the basis of this mixture model, we calculated coordination numbers of four Rh neighbor shells using a fitting parameter, c (a composition for 13-Rh-atom clusters), to obtain the best fitting to the observed coordination numbers. When $c \sim 90\%$, the observed data agree best with the mixture model of small clusters and large particles as shown in Table 4. If we postulate 1.3-nm spherical particles as found in RhY in the pore together with the 3.0-nm particles on the external surface, the coordination numbers for higher shells will be much larger than those found in the EXAFS of Li/RhY for any c. Moreover, such 1.3-nm particles should have been observed in TEM pictures. Thus, most of the Rh atoms are in an Rh cluster as small as 0.8 nm which is smaller than the particle in RhY (1.3 nm). The reason for the smaller particle size in Li/RhY than in RhY may be explained as follows: the size of the supercage is about 1.3 nm in diameter, the same as the size of Rh particles (55 atoms) found in RhY. However, in Li/RhY, Li atoms are also deposited on the walls of the cages. As a result, the effective pore sizes become smaller and 1.3-nm clusters are no longer acceptable, as shown in Fig. 11. This mixture model of a large number of small Rh clusters in the pore together with minor large particles on the external surface is also supported by the hydrogen adsorption measurement and XRD data, both of which indicate only the presence of a smaller cluster. A H/Rh value estimated from this mixture model assuming 90% 13-Rh-atom clusters is nearly 0.86, comparable to the observed value (=0.75). We conclude that most of the Rh particles (90%) exist inside the zeolite

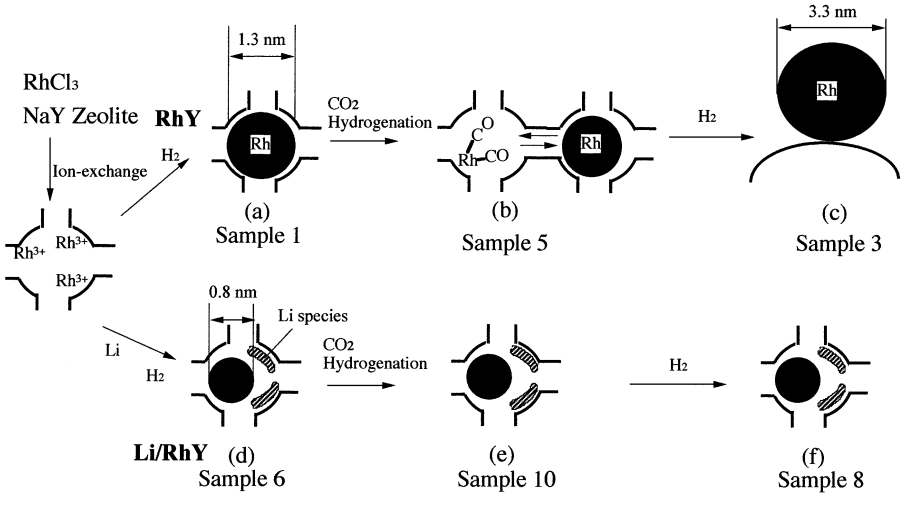

FIG. 11. Proposed structures of Rh particles on RhY and Li/RhY.

cage as small clusters of about 0.8 nm in fresh Li/RhY and a small number of large particles are present on the external surface of the zeolite, which are observed with TEM.

4.1.2. CO adsorption on fresh RhY and Li/RhY. When CO is adsorbed on the Rh particles in RhY, the coordination number of Rh–Rh decreases to 4.2 (sample 2). The decrease in coordination number can be explained by the cleavage of the Rh–Rh bond in Rh particles to form atomically dispersed Rh atoms according to Eq. [3]. Another possible explanation may be that an $Rh_6(CO)_{16}$ cluster is formed in the cage by the reaction with CO. The formation of an Rh carbonyl cluster in NaY is also reported by Ichikawa and Sachtler as a ship-in-a-bottle synthesis (22, 23). The formation of $Rh_6(CO)_{16}$ is supported by the XANES observation; that is, we observed a decrease in the interval of the peaks A and B, which implies the creation of Rh carbonyl species when CO is adsorbed. But if an $Rh_6(CO)_{16}$ cluster were mainly formed in the pore, the Rh–Rh bond length should be 0.01 nm longer than that in Rh metal particles. Table 2 shows only 0.003 nm expansion after CO adsorption. Moreover, a higher shell peak should disappear after CO adsorption if $Rh_6(CO)_{16}$ were created in the pore. Thus, the disruption is assumed to predominantly occur in RhY. Actually, we carried out an *in situ* FT-IR measurement during CO adsorption and observed intense twin CO peaks assigned to dicarbonyl species adsorbed on atomically dispersed Rh species (8). The oscillations due to Rh–CO and Rh–O bonds should be included in EXAFS. However, the Rh–C bond cannot be clearly seen in the Fourier transforms, similarly to the case reported in the literature for Rh carbonyl clusters (24–26). Possibly, a strong Rh–Rh EXAFS oscillation hinders smaller Rh–C and Rh–O contributions.

On the other hand, the particle size of Rh in Li/RhY is maintained after CO adsorption. A small decrease in the coordination number of Rh–Rh is observed along with a small change in the XANES spectrum. Li cations present on the pore surface may prevent the transformation of the Rh particles by hindering reaction [3]. Reaction [3] requires oxidation of Rh by OH groups but the large ionization tendency of Li^+ inhibits the oxidation of Rh by OLi to form Rh^{3+} and Li^0.

4.1.3. Used RhY and Li/RhY. TEM and H_2 adsorption show that the Rh particles in the used RhY catalyst (sample 3) are as large as 3 nm in diameter, which also agrees with the coordination number analyses of EXAFS as shown in Fig. 6. The CO_2 hydrogenation reaction and subsequent reduction bring Rh particles out of the cage and produce larger particles. Such aggregation is also reported in the literature (27). On the other hand, EXAFS analyses of the used Li/RhY (sample 8) show a small increase in coordination numbers as shown in Fig. 10 and Table 2, indicating that CO_2 hydrogenation causes less morphological change in the presence of Li. Li prevents the migration of Rh out from the pores during the reaction.

4.1.4. The structure in the working state. As mentioned above, Li additive affects the behavior of Rh species under the reaction conditions. For Li/RhY (sample 10), the coordination number of the first shell is almost the same as that observed for the fresh catalyst (sample 6), indicating that the Rh clusters are stable in the supercage during the reaction. On the other hand, in the Fourier transform of RhY under the reaction conditions (sample 5), a new peak appears at 0.19 nm, which is determined to be Rh–O bonding. In addition, a significant decrease is found in the coordination number for Rh–Rh bonding. These facts imply that a large number of Rh atoms exist in an atomically dispersed structure together with Rh particles. The redispersion of Rh occurs in a similar way to the CO-induced disruption of Rh particle as mentioned above. During the CO_2 hydrogenation reaction, adsorbed Rh–CO species formed on the surface of Rh particles react with surface OH groups to form the atomically dispersed Rh species in Eq. [3]. In the literature, it is claimed that CO-induced disruption of Rh particles is hindered by the presence of H_2 and that at higher temperatures CO-induced agglomeration rather than disruption will occur (16, 17, 28). However, our work deals with CO_2 hydrogenation under high-pressure conditions, and a significant amount of water was produced and accumulated inside the cages during the reaction, which placed the catalyst surface under oxidative conditions and might promote disruption of Rh particles. Therefore, we think the results obtained for CO hydrogenation or CO adsorption under reduced pressure could not be applicable to our system. In order to get direct evidence, we are now planning to observe the *in situ* EXAFS for the catalysts under the reaction conditions. In conclusion, there are two kinds of Rh species in RhY during the reaction. One is in an atomically dispersed form and the other is a metal cluster in a supercage. Unlike the sample 2 where little contribution of Rh–C to Rh EXAFS was found, a Rh–O bond is more obvious in the process of redispersion by the CO_2 hydrogenation reaction, probably because desorption of CO and further oxidation of Rh by surface O^{2-} or surface H_2O may take place at high temperature during the reaction. The presence of Rh species in a higher oxidation state is supported by the XANES spectra shown in Figs. 8 and 9. Such atomically dispersed Rh species can migrate and the subsequent reduction of RhY produces large Rh particles on the external surface.

In summary, the structures of Rh particles in RhY and Li/RhY are transformed differently during the CO_2 hydrogenation reaction, as shown in Fig. 11.

4.2. Proposed Models and Mechanism

The Li additive significantly modifies the reactivity of the RhY catalysts for CO_2 hydrogenation. The CO_2 molecule is transformed to methane on RhY, while it is transformed mainly to CO on the Li/RhY catalysts. In the literature, the

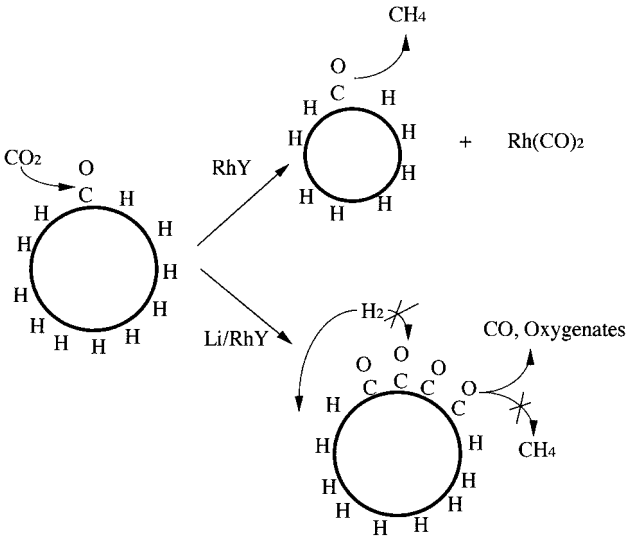

FIG. 12. Proposed mechanism for CO_2 hydrogenation.

possible Li effects are explained by an electronic effect or bifunctional catalysis (29, 30). However, XPS and XANES suggest that the electronic states of Rh are the same for both catalysts. In addition, we cannot find a direct bond between Rh and Li. Therefore, we cannot obtain direct evidence to support these conventional mechanisms.

Here we propose a new mechanism derived from EXAFS observations (Fig. 12), based on dynamic structures formed during the CO_2 hydrogenation reaction. H_2 can be adsorbed on the Rh surface more easily than CO_2 and the surface hydrogen concentration is high in the initial stage of the reaction. CO_2 easily reacts with neighboring hydrogen to form CO, which is then converted to methane through subsequent reaction with predominantly adsorbed hydrogen. As a reaction proceeds, CO adsorbates will be accumulated on the surface to from a CO island if the CO hydrogenation step is not as fast as the conversion of CO_2 to CO. Once the CO island is formed, hydrogenation of adsorbed CO ceases inside the CO island because of the inhibition of hydrogen adsorption by the strongly adsorbed CO. Since CO adsorbates can be supplied by the reaction with adsorbed CO_2 and hydrogen from the periphery of the CO island, the CO islands grow at an accelerated rate and finally cover the whole surface of the Rh particles. Consequently, adsorption of hydrogen on Rh particles is suppressed and methane formation is deactivated, CO being found as a main product. The hydrogenation reaction may occur on the CO domain very slowly to form CH_3, CH_2, and CHOH groups. These species react with surrounding CO to form acyl species, and ethanol may be preferably created. This may be the case in Li/RhY. In RhY, on the other hand, when CO accumulation occurs on the RhY surface, the adsorbed Rh–CO species reacts with OH groups and is liberated from the Rh particles to form atomically dispersed Rh species. Accordingly, CO islands cannot be formed on the Rh particles and the surface hydrogen concentration on the Rh particle is kept high, so that CO_2 and CO hydrogenation reactions proceed to form methane. The dispersed Rh species is slowly reduced and is returned to the Rh particle. In this proposed mechanism, the presence of Li additive controls the dynamic change of the Rh particle structure, which brings about the different catalytic reactivity. To establish the reaction mechanism including dynamic change of active sites it is necessary to carry out time-resolved experiments in IR and EXAFS to correlate the change of the particle structure and catalytic activity as well as to study surface kinetics.

5. CONCLUSION

The transformation of Rh particles on Rh ion-exchanged zeolite catalysts (RhY) and that on Li-doped RhY catalysts (Li/RhY) were studied by TEM and EXAFS.

(1) For the RhY catalysts, Rh particles have a relatively fragile character. Initially Rh atoms are present in 1.3-nm particles inside the zeolite cages. During the reaction, some of them are atomically dispersed and others remain as particles. By subsequent reduction, they aggregate to 3.3-nm particles.

(2) For Li/RhY, Rh particles are tightly embedded inside the cage surrounded by Li atoms. The structure of the Rh particles is almost the same before, during, and after the reaction.

(3) CH_4 is a main product in RhY, because the surface concentration of CO on Rh particles is kept small by CO-induced disruption of Rh particles into atomically dispersed Rh species with which CO is liberated from the Rh particles. In Li/RhY, since adsorbed CO species are accumulated on the surfaces of stable Rh particles, CO production mainly occurs.

REFERENCES

1. Arakawa, H., *Stud. Suf. Sci. Catal.* **114**, 19 (1998).
2. Preville, M. A., and Koch, H. J., *Stud. Surf. Sci. Catal.* **114**, 1 (1998)
3. Bhasin, M. M., Barley, W. J., and Wilson, P. C., *J. Catal.* **54**, 120 (1978).
4. Solymosi, F., Erdohelyi, A., and Bansagi, T., *J. Catal.* **68**, 371 (1981).
5. Fisher, I. A., and Bell, A. T., *J. Catal.* **162**, 54 (1996).
6. Iizuka, T., Tanaka, Y., and Tanabe, K., *J. Catal.* **76**, 1 (1982).
7. Inoue, T., Iizuka, T., and Tanabe, K., *Appl. Catal.* **46**, 1 (1989)
8. Bando, K. K., Soga, K., Kunimori, K., Ichikuni, N., Okabe, K., Kusama, H., Sayama, K., and Arakawa, H., *Appl. Catal. A General* **173**, 47 (1998).
9. Arakawa, H., Hanaoka, T., Takeuchi, K., Matsuzaki, T., and Sugi, Y., *in* "Proceedings, 9th International Congress on Catalysis, Calgary, 1988" (M. J. Phillips and M. Teran, Eds.), p. 602. Chem. Institute of Canada, Ottawa, 1988.
10. Kusama, H., Okabe, K., Sayama, K., and Arakawa, H., *Catal. Today* **28**, 261 (1996).
11. Bando, K. K., Soga, K., Kunimori, K., and Arakawa, H., *Appl. Catal. A: General* **175**, 67 (1998).
12. Liotta, L. F., Martin, G. A., and Deganello, G., *J. Catal.* **164**, 322 (1996).

13. Asakura, K., *in* "X-ray Absorption Fine Structure for Catalysts and Surfaces" (Y. Iwasawa, Ed.), 1st ed., Vol. 2, p. 33. World Scientific, Singapore, 1996.
14. Van't Blik, H. F. J., Van Zon, J. B. A. D., Huizinga, T., Vis, J. C., Koningsberger, D. C., and Prins, R., *J. Phys. Chem.* **87**, 2264 (1983); Van't Blik, H. F. J., Van Zon, J. B. A. D., Huizinga, T., Vis, J. C., Koningsberger, D. C., and Prins, R., *J. Am. Chem. Soc.* **107**, 3139 (1985).
15. Solymosi, F., and Pasztor, M., *J. Phys. Chem.* **89**, 4789 (1985); Solymosi, F., Pasztor, M., *J. Phys. Chem.* **90**, 5312 (1986).
16. Solymosi, F., and Bansagi, T., *J. Phys. Chem.* **97**, 10133 (1993).
17. Berko, A., and Solymosi, F., *J. Catal.* **183**, 91 (1999).
18. Tzuo, M.-S., Kusunoki, M., Asakura, K., Kuroda, H., Moretti, G., and Sachtler, W. M., *J. Phys. Chem.* **95**, 5210 (1991).
19. Zhang, Z., Chen, H., Sheu, L.-L., and Sachtler, W. M. H., *J. Catal.* **127**, 213 (1991).
20. Tomishige, K., Asakura, K., and Iwasawa, Y., *Catal. Lett.* **20**, 15 (1993).
21. Tomishige, K., Asakura, K., and Iwasawa, Y., *J. Catal.* **149**, 70 (1994).
22. Rao, L.-F., Fukuoka, A., Kosugi, N., Kuroda, H., and Ichikawa, M., *J. Phys. Chem.* **94**, 5317 (1990).
23. Trevino, H., Lei, G.-D., and Sachtler, W. M. H., *J. Catal.* **154**, 245 (1995).
24. Asakura, K., Iwasawa, Y., and Kuroda, H., *Bull. Chem. Soc. Jpn.* **59**, 647 (1986).
25. Izumi, Y., and Iwasawa, Y., *J. Phys. Chem.* **96**, 10942 (1992).
26. Ichikawa, M., Imada, Y., Yamaguchi, M., and Isobe, K., *J. Mol. Catal.* **107**, 23 (1996).
27. Shunemann, V., Trevino, H., Lei, G. D., Tomczak, D. C., Sachtler, M. H., Fogash, K., and Dumesic, J. A., *J. Catal.* **153**, 144 (1995).
28. Berko, A., Menesi, G., and Solymosi, F., *J. Phys. Chem.* **100**, 17732 (1996).
29. Kazi, A. M., Chen, B., Goodwin, Jr., J. G., Marcelin, G., Rodriguez, N., R. Terry, R., and Baker, K., *J. Catal.* **157**, 1 (1995).
30. Millar, G. J., Rochester, C. H., and Waugh, K. C., *J. Catal.* **155**, 53 (1995).